

Strong Coulomb effects on pions produced in heavy ion collisions

J. P. Sullivan,* J. A. Bistirlich, H. R. Bowman, R. Bossingham, T. Buttke,
K. M. Crowe, K. A. Frankel, C. J. Martoff,[†] J. Miller,[‡] D. L. Murphy,
J. O. Rasmussen, and W. A. Zajc

*Nuclear Science Division, Lawrence Berkeley Laboratory, University of California,
Berkeley, California 94720*

O. Hashimoto and M. Koike

*Institute for Nuclear Study, University of Tokyo, Tanashi, Tokyo 188, Japan
and Nuclear Science Division, Lawrence Berkeley Laboratory, University of California,
Berkeley, California 94720*

J. Péter

Institut de Physique Nucléaire, B. P. No. 1, 91406 Orsay Cedex, France

W. Benenson, G. M. Crawley, E. Kashy, and J. A. Nolen, Jr.

Michigan State University, East Lansing, Michigan 48824

(Received 1 July 1981)

Doubly differential cross sections for the production of π^+ and π^- near the velocity of the incident beam for pion laboratory angles from 0 to 20 degrees are presented. Beams of ^{20}Ne with $E/A=280, 380,$ and 480 MeV and ^{40}Ar with $E/A=535$ MeV incident on C, NaF, KCl, Cu, and U targets were used. A sharp peak in the π^- spectrum and a depression in the π^+ spectrum is observed at 0° near the incident projectile velocity. The effect is explained in terms of Coulomb interactions between pions and fragments of the incident beam. Least squares fits to the data using the Coulomb correction formulas of Gyulassy and Kauffmann and an effective projectile fragment charge are made. The relationship between these data and previously measured projectile fragmentation data is discussed and a simple parametrization of projectile mass, target mass, and beam energy dependence of the differential cross sections is given.

NUCLEAR REACTIONS C, NaF, Cu, U ($^{20}\text{Ne}, \pi^\pm$)X, E/A
 $=280-480$ MeV; C, KCl ($^{40}\text{Ar}, \pi^\pm$)X, $E/A=535$ MeV; measured
 $\sigma(E_\pi, \theta_\pi)$, $\theta_\pi=0^\circ-20^\circ$, π velocity near beam velocity; deduced projec-
 tile fragment charges, Coulomb effects.

I. INTRODUCTION

The mechanism of pion production with heavy ion beams has been the subject of considerable recent experimental and theoretical effort. Much of this interest arose from the hope of investigating long-range coherent effects in the nucleus or of probing the early stages of the interaction of two high energy heavy ions. Previous measurements of charged pion production generally showed a smooth dependence on pion momentum. However, most of these experiments were restricted to laboratory angles of 30° or greater¹⁻⁴ or measured only relatively high energy pions.⁵ Streamer chamber

measurements⁶ of π^- cross sections cover forward angles, but beam velocity structure was not noted, perhaps because the number of events measured was too small. More recent measurements⁷ near 0° showed a strong peak in the π^- energy spectrum near the beam velocity and a corresponding dip in the π^+ spectrum. This work has helped stimulate theoretical treatments which showed the essential role of Coulomb effects due to the projectile remnants in producing this pion structure.⁸⁻¹¹ A large π^-/π^+ ratio has been observed previously near the target (lab) velocity in emulsion experiments with proton^{12,13} and alpha¹⁴ beams and with cosmic rays.¹⁵

The analysis of these experiments showed that detailed measurements of π^- and π^+ differential production cross sections could probe the dynamics of charge density evolution in heavy ion collisions. In order to make more accurate and higher resolution measurements, the detection system employed in the earlier work was improved by using two three-plane multiwire proportional counters, one near the focal plane of the spectrometer and one behind it. The pions were stopped in a large-area 11-element scintillation range telescope after passing through the wire chambers.

In the discussion below we describe a series of measurements at beam energies per nucleon between 280 and 535 MeV. The measurements were performed near 0° and for pions near the beam velocity. Beams of ^{40}Ar and ^{20}Ne were used, and the targets ranged from C to U. The results for every case show a very strong Coulomb effect in the π^-/π^+ ratio. Theoretical calculations are also presented which successfully reproduce the Coulomb effects.

II. APPARATUS AND DATA ANALYSIS

A. Apparatus

The data reported in this work were all collected at the Berkeley BEVALAC. Beams of ^{20}Ne with E/A from 280 to 480 MeV and ^{40}Ar with $E/A = 535$ MeV were used. The targets used were C, NaF (mass numbers are approximately equal to ^{20}Ne), KCl (mass numbers are approximately equal to ^{40}Ar), Cu, and ^{238}U . The target thicknesses were between 0.4 and 1.1 g/cm². A schematic diagram of the apparatus used is shown in Fig. 1. The target was located between the coils of the dipole magnet which was used as a pion spectrometer. This target position was chosen to achieve a good 180° focal plane at the position of the first of two multiwire proportional counters (MWPC's) which were used to measure the trajectories of particles in the magnetic field. The second MWPC was followed by a stack of 11 plastic scintillators which was capable of stopping pions with kinetic energies up to 100 MeV. The first two scintillators were thin (0.64 cm) and were used to measure the rate of energy loss of the particles. The pions of interest were then stopped in one or another of the next eight elements of the scintillator stack (2.5–3.8 cm thick). The last scintillator in the stack was 1.3 cm thick and was used as a veto counter. For each event, the addresses of all wires

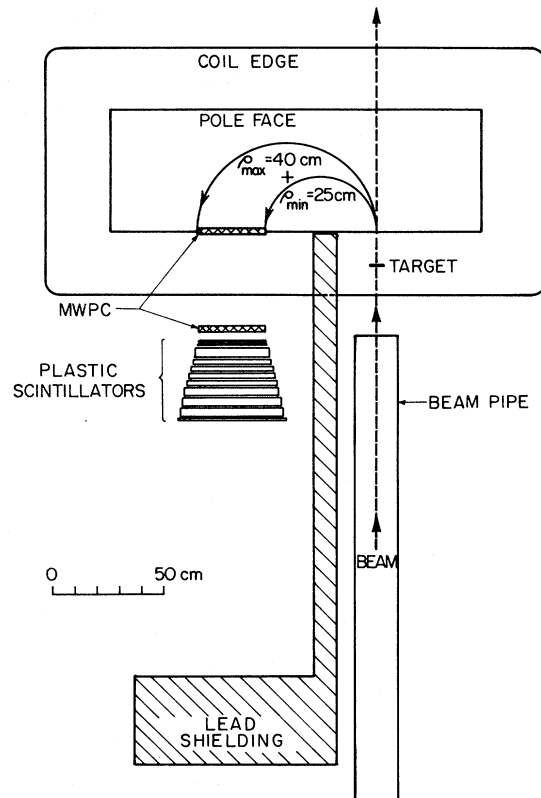


FIG. 1. Schematic diagram of the apparatus.

which were hit and the pulse heights [analog-to-digital converters (ADC's)] and timing signals [time-to-digital converters (TDC's)] from each element of the scintillator stack were recorded on magnetic tape. The data were read by a PDP 11/45 computer from CAMAC using a microcomputer interface (MBD-11).

B. Data reduction

A field map of all three components of the magnetic field of the spectrometer magnet was measured in order to calculate pion orbits in the magnet, and thus to find the positions at which these orbits would cross the MWPC planes. A Monte Carlo program was used to generate the starting parameters of the trajectories. A fit was then made which provides the radius of curvature (ρ), the angle (θ), and the vertical position of the particle at the target (Z_0) as a Chebychev polynomial function of the wire chamber hit positions. The fitting method is described by Alder *et al.*¹⁶ Energy loss of pions in air and the MWPC's was included in the orbit calculations, so this small

($\leq 1.5\%$) correction was included in the algorithm used to calculate ρ , θ , and Z_0 .

For each event on magnetic tape, the addresses of the MWPC wires which fired were used to find the trajectories. If a single trajectory was found, the algorithm described above was used to calculate ρ , θ , and Z_0 for the particle. Some events (approximately 20%) were rejected because these calculated quantities indicated that the event did not come from the target. Momentum-dependent cuts on the energy loss in the first and second scintillators and on the range of the particle in the scintillator stack were then used to identify pions. Protons and electrons were clearly separated from the pions. The muon contamination was estimated to be less than 3% in all cases.

C. Efficiency and acceptance of the spectrometer

The acceptance and efficiency of the spectrometer were calculated with the same Monte Carlo program which was used to generate events for the polynomial fits. Pion events were generated with a uniform distribution in momentum space, and a Gaussian beam spot approximately the size of the actual beam spots was assumed. Pions were allowed to decay into muons while going through the spectrometer (with the appropriate half-life). If a decay did occur, the muon was followed through the spectrometer. When the calculated orbit of a pion or muon passed through both MWPC's and then hit the first scintillator in the range stack, a multiple-scattering, energy loss code was used to follow the particle through the scintillator stack. Pions were allowed to react with carbon nuclei in the scintillators using analytic approximations to the π -C total cross sections given by Carrol *et al.*¹⁷ This total π -C reaction cross section was divided into $\frac{1}{3}$ elastic scattering, $\frac{1}{3}$ inelastic scattering, and $\frac{1}{3}$ pion absorption [treated as a $C(\pi,p)X$ reaction]. The correction due to reactions of pions with carbon nuclei was generally less than 10%, and, since the correction due to reactions with hydrogen is less, the error introduced by ignoring πp reactions should be small. For each Monte Carlo event, the MWPC wires that would be expected to fire were found from the calculated hit positions. A probability distribution taken from the real data was used to decide how many adjacent wires would fire in each MWPC plane. Any wire that was not working during the experiment was then removed from this list of wires. This procedure allows the

MWPC efficiency to be incorporated into the acceptance calculation. The expected ADC signal in each scintillator was estimated from the calculated energy losses. These simulated data were then analyzed in the same manner as the real data.

Since the Monte Carlo events were generated with a probability proportional to dp^3 , dividing the number of real data events in each bin corrected for blank target background by the number of Monte Carlo events gives the differential cross section $d^3\sigma/dp_\pi^3$ except for the overall factor which converts the relative yield into the cross section. The cross section so determined thus includes corrections due to π - μ decay, wire chamber inefficiency, π reactions with C nuclei in the scintillators, multiple-Coulomb scattering in the scintillators, effects due to the finite size of the beam spot, and any inefficiencies in the analysis program. The statistical uncertainty associated with the Monte Carlo was never larger than 5% and has been included in the quoted statistical errors.

D. Normalization

The beam intensity was monitored with an Ar-CO₂-filled ion chamber. In order to reduce the background associated with the beam hitting the ion chamber, the chamber was placed at the last beam focal point prior to the target, 13 m upstream. The transmission of the beam from the ion chamber through the final pair of quadrupole focusing magnets to the target position was measured with plastic scintillators at reduced beam intensity and with a second ion chamber. The ion chamber was calibrated as described in the previous experiment.⁷ Using the ion chamber, the total number of beam particles could be calculated and the cross-section values normalized. We estimate a 30% uncertainty in the absolute normalization. The factors contributing to this uncertainty are listed in Table I.

Secondary reactions of pions or the beam in the target and effects due to neutrons from capture of stopped negative pions by nuclei in the scintillator stack were neglected. The correction due to secondary reactions would increase the π^+ and π^- cross sections by less than 3%. The correction due to stopped negative pions would increase the π^- cross sections by less than 10%.

In addition to the present data, we obtained a small amount of data for $^{20}\text{Ne} + \text{NaF}$ at $E/A = 400$ MeV. These 400 MeV data were taken at larger laboratory angles than the data presented

TABLE I. Normalization and correction factors and their uncertainties.

Factor	Typical value	Estimated uncertainty ^f
Beam intensity		± 25
Computer dead time	20	± 5
MWPC inefficiency	5–10	± 3
Events rejected because they did not trace back to the target ^a	20	± 6
dE/dx cuts ^b	5–10	± 3
Range cuts ^c	15–40	± 10
Spectrometer acceptance ^d		± 10
Overall uncertainty ^e		± 30

^aThese events were rejected because the trajectory did not trace back to the target; many of the muons from decay in flight of pions are rejected by this cut.

^bCuts on the energy loss (dE/dx) in the first two scintillators.

^cCuts on the range of the particle in the scintillator stack.

^dThis includes uncertainties in the calculation itself, in the field map, and in the target and detector positions.

^eCalculated by combining all uncertainties in quadrature.

^fThe estimated uncertainty in the overall normalization due to the factor, e.g., computer dead time correction was $20 \pm 5\%$.

here, and overlap both our $\text{Ne} + \text{NaF} \rightarrow \pi^+$ data at $E/A = 380$ MeV (close to 400 MeV) and the data of Nakai *et al.*³ at larger laboratory angles. Using this set of data to extrapolate the π^+ data reported here, we found that their cross sections are about 30% higher than our present results, and there is good agreement between the slope of cross section versus momentum. The 30% disagreement is within the limits of error on both their absolute normalization and ours. Our results are also 30% lower than those of Nagamiya *et al.*,¹ but their normalization may not be independent of Nakai *et al.* since the two sets of data were collected simultaneously with common beam monitors. The normalization of another set of π^+ data taken with this apparatus¹⁸ agrees with the normalization of Wolf *et al.*⁴ for $^{40}\text{Ar} + ^{40}\text{Ca}$ at $E/A = 1.05$ GeV. When we compare our new cross sections with those of our earlier work with the Pb-slit-scintillator spectrometer,⁷ we find that the absolute value of the present results is about 50% of that obtained previously, which is within the quoted uncertainty.

E. Resolution

In comparing cross sections with sharp structure one must take experimental resolution into account. The beam velocity peaks and valleys of the data have widths larger than the resolution, but effects due to the resolution cannot be ignored. This effect was treated by folding the calculated resolution function into the theoretically calculated cross sections. Factors contributing to the resolution were the size of the beam spot; the spatial resolution of the MWPC's; energy loss in the target; multiple scattering in the target, in air, and in the MWPC's; the size of the data bins; and the uncertainty introduced by the use of the polynomial fit to calculate the momenta of the particles. Multiple scattering in the target made the largest contribution to the angular resolution. The momentum resolution was not dominated by any single effect. Table II summarizes the resolution of the spectrometer for pions near the momentum of the observed peaks in the negative pion spectra for the combinations of beam energies and target reported

TABLE II. Summary of experimental parameters.

Beam	Beam energy per nucleon (MeV)		Target material	Target thickness (g/cm ²)	Pion momentum with velocity of incident beam (MeV/c)	Resolution ^b	
	at accelerator	at center of target ^a				σ_p (%)	σ_θ (deg)
²⁰ Ne	300	280	C	0.56	116	2.2	2.0
		281	NaF	0.60	116	2.2	2.1
		282	Cu	0.45	117	2.3	2.4
²⁰ Ne	400	380	NaF	1.07	138	2.1	2.2
		382	Cu	0.91	139	2.0	2.6
		385	U	0.52	139	2.2	2.9
²⁰ Ne	500	482	C	1.12	159	1.5	1.9
		483	NaF	1.07	160	1.4	2.0
		485	Cu	0.91	160	1.4	2.2
		487	U	0.52	160	1.6	2.4
⁴⁰ Ar	557	533	C	0.56	169	1.4	1.7
		534	KCl	0.50	170	1.4	1.8

^aThe beam energy at the center of the target is less than the energy at the exit of the accelerator due to energy loss in material in the beam line as well as energy loss in the target. These beam energies were measured as described in Ref. 19.

^bThe resolution is defined as the rms difference between the calculated momentum or angle and the true value.

here.

Due to uncertainties in the absolute magnitude of the magnetic field used during the experiment and the position of the beam spot on the target, there is an additional 1.5% uncertainty in the magnitude of the momentum. The beam ranges were measured with aluminum and/or copper wedges and Polaroid film, and the beam energies were calculated from the ranges.¹⁹ All beam and pion energies given here are the values at the center of the target.

III. RESULTS

Figures 2–5 show cuts through the peak in the π^- spectra (hole in the π^+ spectra) as a function of laboratory angle and laboratory momentum for each of the nearly equal mass projectile-target combinations studied. The vertical error bars are statistical. The horizontal error bars on the graphs of cross section versus angle show the angular resolution (given in Table II) and, on the graphs of cross section versus momentum, show the momentum resolution. The solid curves are least squares fits of functions based on Gyulassy and Kauffmann's¹⁰ theoretical expressions. These solid curves have had the resolution of the spectrometer

folded into them. The dashed curves are the same functions before folding with the resolution and the dotted curves are the fitted pion spectra in the absence of Coulomb effects. Figures 6–17 show the data for all projectile-target combinations studied as plots of Lorentz invariant cross sections versus laboratory momentum at fixed laboratory angles from 0 to 20 deg. As in Figs. 2–5, the vertical error bars are statistical and the solid curves are least squares fits with the experimental resolution folded in. Numerical tables of all cross sections will be given in Ref. 20.

In the case of the π^+ data at $E/A=380$ MeV, we have an overlap with Nakai *et al.*³ As mentioned earlier, there is a 30% disagreement in normalization. We therefore apply this normalization factor to their data and combine it with our data to produce the Lorentz-invariant cross section contour plot of Fig. 18. Here the approximate symmetry about the center of mass has been used to reflect the data sets of both studies about the center of mass.

For all the projectile-target combinations which were studied, a peak in the π^- differential cross section (and in the π^-/π^+ ratio) was observed slightly lower than the velocity of the incident beam. The shifts of the peaks from the momen-

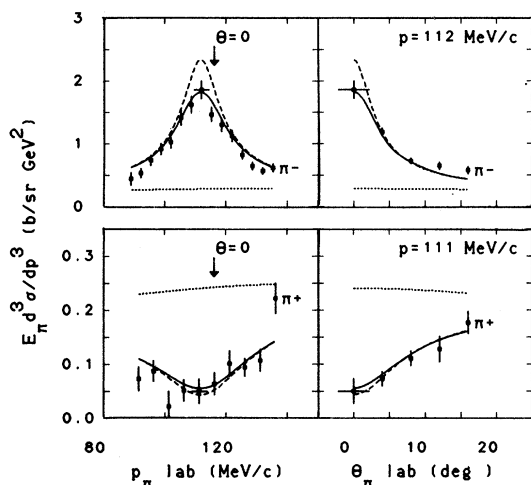


FIG. 2. Lorentz invariant cross section cuts for $\text{Ne} + \text{NaF} \rightarrow \pi^\pm$ at $E/A=281$ MeV. The left side of the graph shows the cross section versus momentum at 0 degrees in the laboratory for π^- (top) and π^+ (bottom). The right side shows the cross section versus laboratory angle at a fixed laboratory momentum near the peak in the π^- spectrum. The solid line is from a least squares fit of a function based on the Coulomb correction equations of Gyulassy and Kauffmann (Ref. 10). This solid line has the experimental resolution folded into it. The dashed line is the same function before folding with the resolution. The dotted line shows the cross section predicted by the uncharged pion source function to which the Coulomb corrections were applied. The arrows on the left-hand graphs mark the velocity of the incident beam.

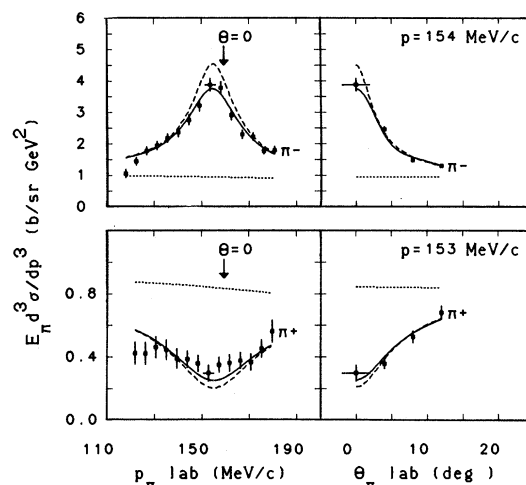


FIG. 4. Lorentz invariant cross section cuts for $\text{Ne} + \text{NaF} \rightarrow \pi^\pm$ at $E/A=483$ MeV. See also the caption for Fig. 2.

tum associated with the beam velocity are, within our experimental uncertainties, independent of beam energy over the range reported here. For the neon beam this pion momentum shift is 3.2 ± 1.6 MeV/c in the rest frame of the incident beam. For ^{40}Ar the corresponding shift is 2.0 ± 1.7 MeV/c. The depression in the π^+ cross section near beam velocity is broader than the corresponding π^- peak but has approximately the same downshift as does the π^- peak.

Table III gives the half-widths, $\Gamma_i/2$, of the peaks in the π^- spectra and the pion momentum

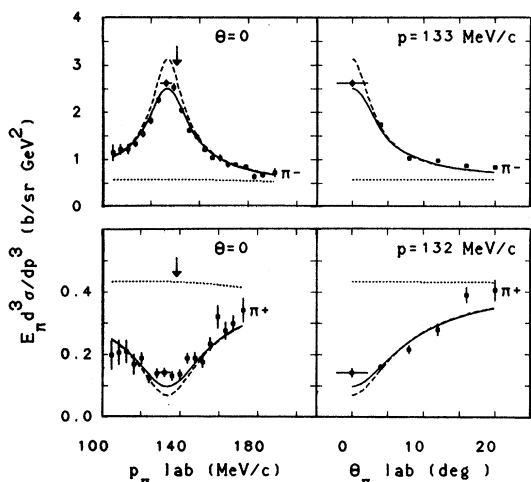


FIG. 3. Lorentz invariant cross section cuts for $\text{Ne} + \text{NaF} \rightarrow \pi^\pm$ at $E/A=380$ MeV. See also the caption for Fig. 2.

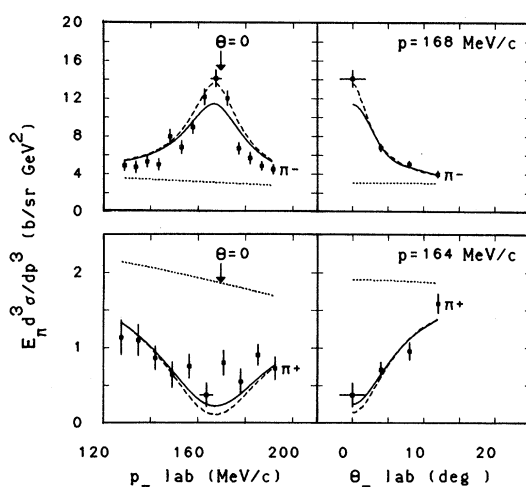


FIG. 5. Lorentz invariant cross section cuts for $\text{Ar} + \text{KCl} \rightarrow \pi^\pm$ at $E/A=534$ MeV. See also the caption for Fig. 2.

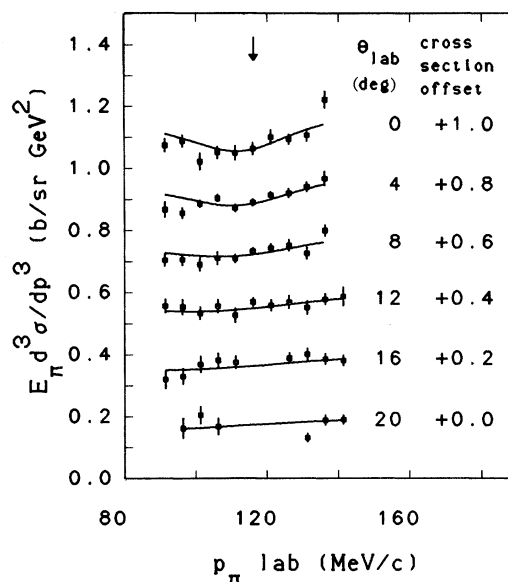
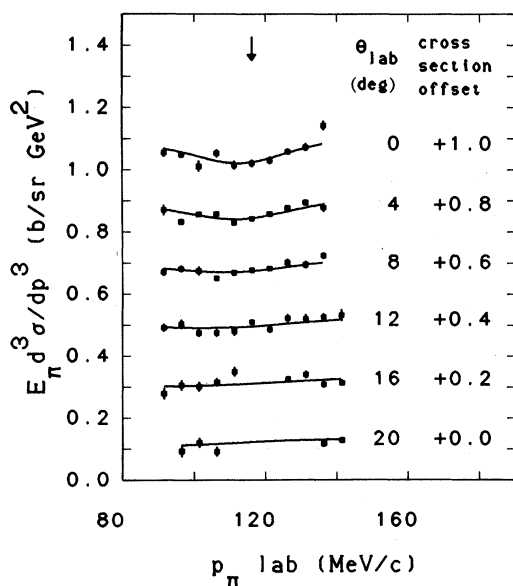
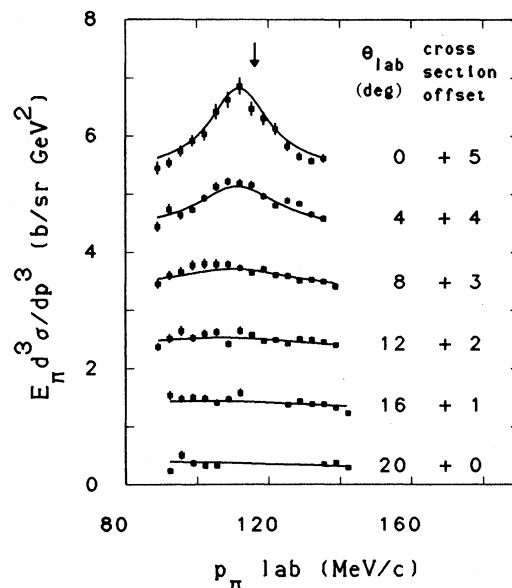
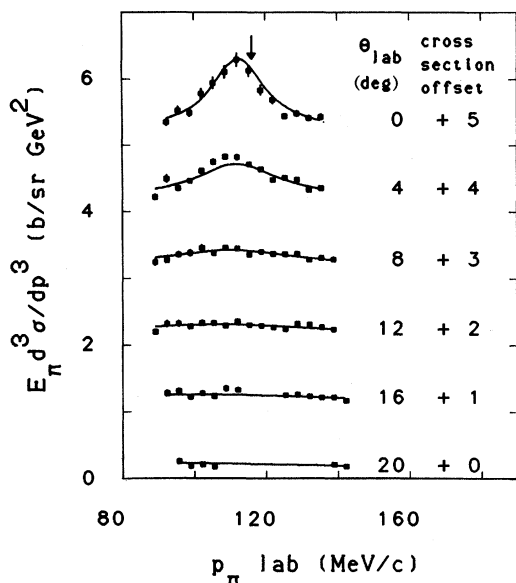


FIG. 6. Lorentz invariant cross section versus laboratory momentum for (a) $\text{Ne} + \text{C} \rightarrow \pi^-$ at $E/A=280$ MeV, and (b) $\text{Ne} + \text{C} \rightarrow \pi^+$ at $E/A=280$ MeV. Each set of points is at a fixed laboratory angle, which is shown on the right side of the figure. A cross section offset has been added to the data at each angle (except the 20 degree data) in order to display it all on the same graph. This offset is given on the right side of the figure. The solid line is from a least squares fit of a function based on the Coulomb correction equations of Gyulassy and Kauffmann (Ref. 10). This function has been folded with the resolution of the spectrometer. The arrow marks the velocity of the incident beam.

FIG. 7. Lorentz invariant cross section versus laboratory momentum for (a) $\text{Ne} + \text{NaF} \rightarrow \pi^-$ at $E/A=281$ MeV and (b) $\text{Ne} + \text{NaF} \rightarrow \pi^+$ at $E/A=281$ MeV. See also the caption for Fig. 6.

shifts for each of the projectile-target combinations in the projectile velocity frame. The widths are defined as the half-widths at half-maximum, measured above a smooth background. The smooth background was defined by the source function which is described below [see Eq. (4)]. The resolution of the spectrometer has been subtracted in quadrature from these widths. In Table III the

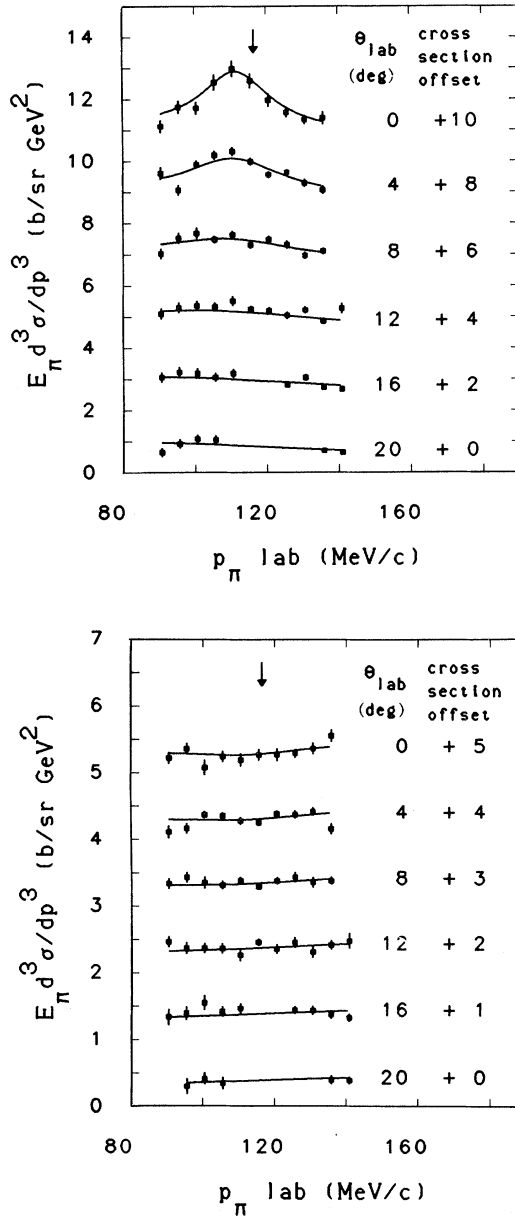


FIG. 8. Lorentz invariant cross section versus laboratory momentum for (a) $\text{Ne} + \text{Cu} \rightarrow \pi^-$ at $E/A = 282$ MeV and (b) for $\text{Ne} + \text{Cu} \rightarrow \pi^+$ at $E/A = 282$ MeV. See also the caption for Fig. 6.

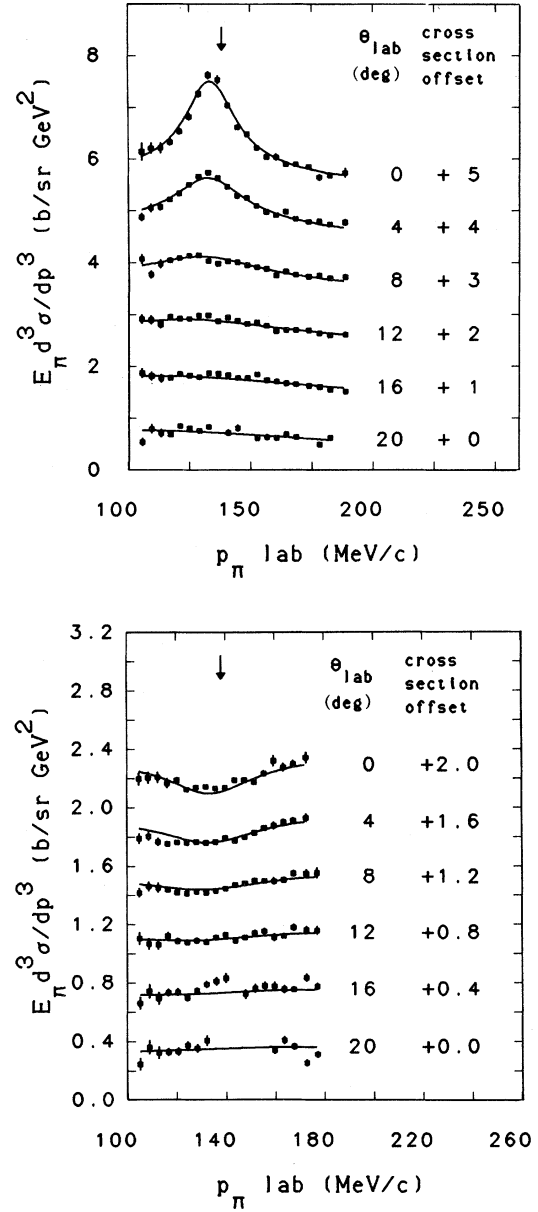


FIG. 9. Lorentz invariant cross section versus laboratory momentum for (a) $\text{Ne} + \text{NaF} \rightarrow \pi^-$ at $E/A = 380$ MeV and (b) for $\text{Ne} + \text{NaF} \rightarrow \pi^+$ at $E/A = 380$ MeV. See also the caption for Fig. 6.

widths of the peaks are expressed in terms of parallel and perpendicular momentum; if they had been defined in terms of pion kinetic energies in the beam velocity reference frame, the full widths at half-maximum would generally be less than 1 MeV.

IV. DISCUSSION

A. Coulomb correction equations

The theory of Gyulassy and Kauffmann¹⁰ (GK) has been used to fit the π^{\pm} data. In their work,

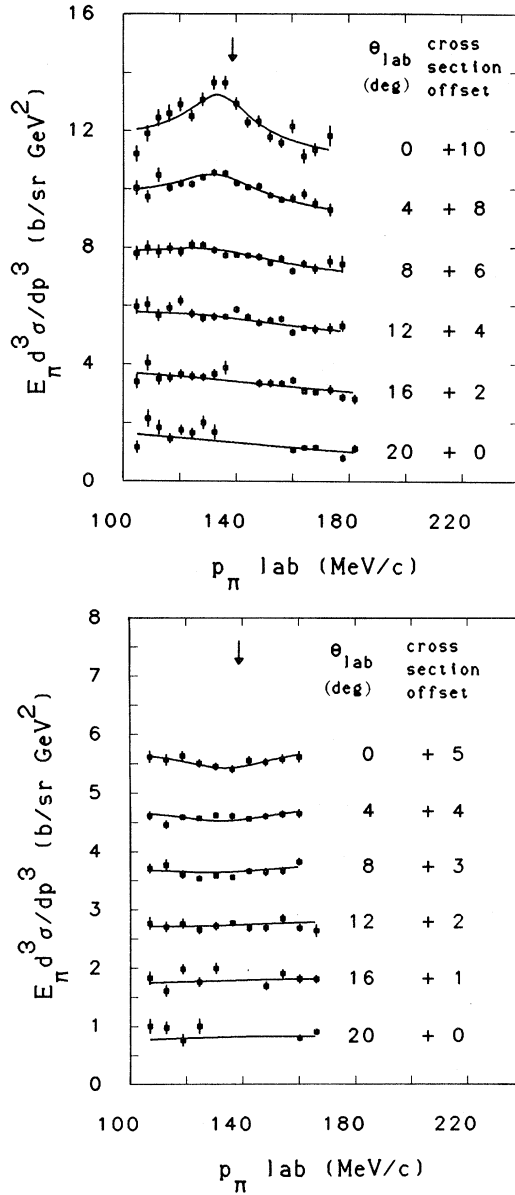


FIG. 10. Lorentz invariant cross section versus laboratory momentum for (a) $\text{Ne} + \text{Cu} \rightarrow \pi^-$ at $E/A=382$ MeV and (b) for $\text{Ne} + \text{Cu} \rightarrow \pi^+$ at $E/A=382$ MeV. See also the caption for Fig. 6.

approximate Coulomb correction formulas are developed, using a perturbative approach to treat both quantum and relativistic effects due to the field of thermally expanding charge distributions. The charged pion cross sections are given in terms of an uncharged pion cross section evaluated at a momentum which has been shifted by a Coulomb impulse, then modified by a Coulomb phase space distortion factor. The “nonperturbative” extrapolation of the GK model has been used in this

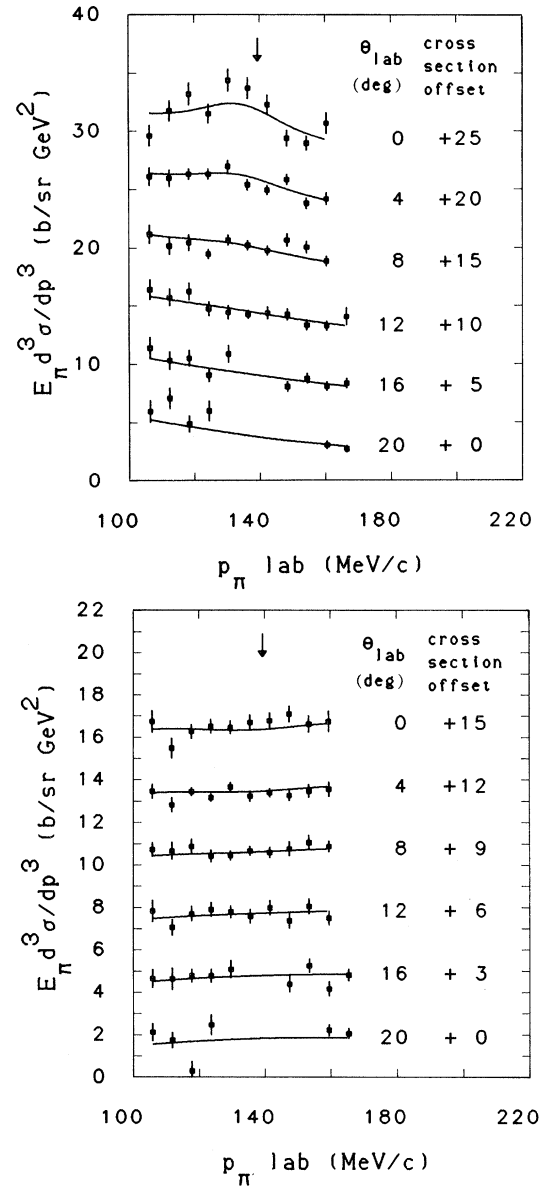


FIG. 11. Lorentz invariant cross section versus laboratory momentum for (a) $\text{Ne} + \text{U} \rightarrow \pi^-$ at $E/A=385$ MeV and (b) for $\text{Ne} + \text{U} \rightarrow \pi^+$ at $E/A=385$ MeV. See also the caption for Fig. 6.

analysis.

$$\sigma_{\pm}(\vec{p}) = \sigma_0(\vec{p} \mp \delta\vec{p})G(\pm\delta D/\pi), \quad (1)$$

where $\sigma_0(\vec{p})$ is the uncharged pion source function ($d^3\sigma/dp^3$), \vec{p} is the observed momentum of the particle, $\delta\vec{p}$ is the Coulomb impulse, δD is the Coulomb phase space distortion factor, and $G(\eta) = 2\pi\eta / [\exp(2\pi\eta) - 1]$ with $\eta = Z\alpha/\beta$. The uncharged pion source function is evaluated at a shifted momentum, and the momentum shift is

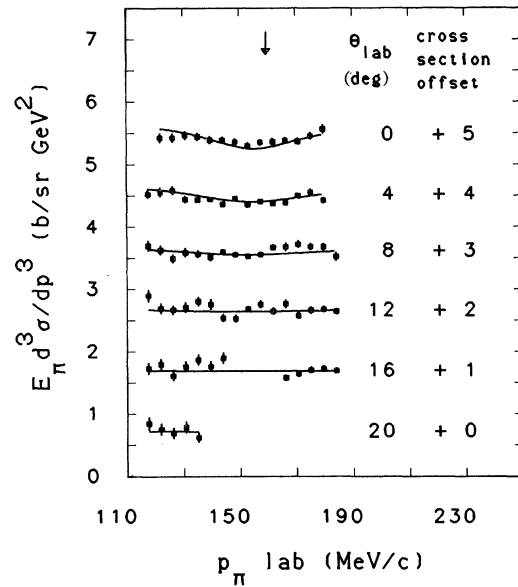
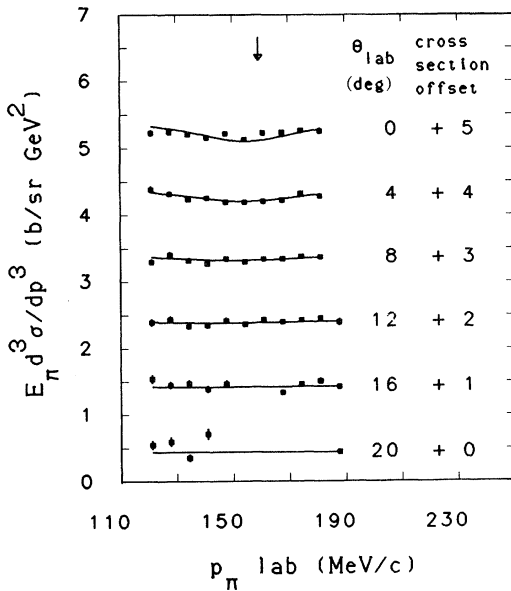
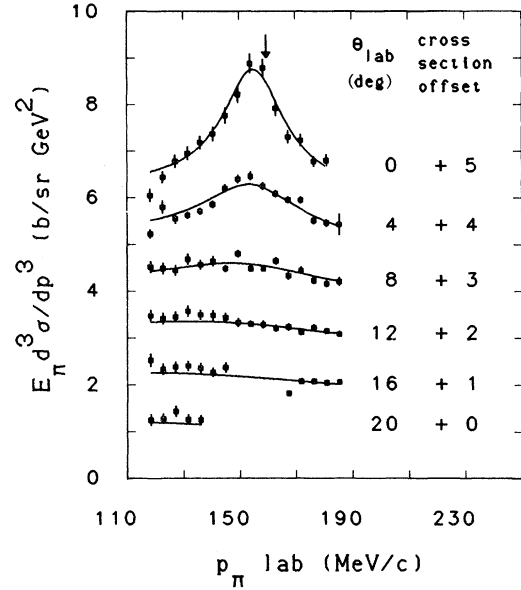
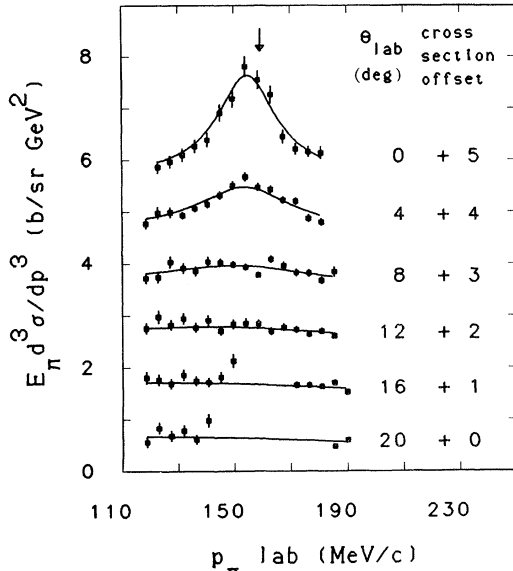


FIG. 12. Lorentz invariant cross section versus laboratory momentum for (a) $\text{Ne} + \text{C} \rightarrow \pi^-$ at $E/A=482$ MeV and (b) for $\text{Ne} + \text{C} \rightarrow \pi^+$ at $E/A=482$ MeV. See also the caption for Fig. 6.

FIG. 13. Lorentz invariant cross section versus laboratory momentum for (a) $\text{Ne} + \text{NaF} \rightarrow \pi^-$ at $E/A=483$ MeV and (b) for $\text{Ne} + \text{NaF} \rightarrow \pi^+$ at $E/A=483$ MeV. See also the caption for Fig. 6.

given by GK as

$$\delta \vec{p}_\mu(\vec{p}) = \sum_i Z_i \alpha(q - E'_i u_i / c)_\mu \times \frac{E'_i R_i \hbar c}{(\hbar c)^2 + (p'_i c R_i)^2}, \quad (2)$$

where the parameters associated with the charged fragments are the following: Z_i is the charge on fragment i ; $R_i = \langle 1/r \rangle^{-1}$ is the mean inverse ra-

dius of fragment i ; T_i is the temperature of fragment i in MeV; $\beta_{Ti}^2 = \pi T_i / 2m_p c^2 = T/597$ MeV is the mean square thermal velocity of protons; $u_i = 4$ -velocity of fragment $i = (\gamma_i, \gamma_i \vec{\beta}_i)$; $\gamma_i = (1 - \beta_i^2)^{-1/2}$. The kinematic variables are the following: E_i is the energy of a particle in the rest frame of charge i (mass + kinetic) $= q_\mu u_i^\mu = (E/c) \gamma_i - \vec{p} \cdot \vec{u}_i$; $E'_i = E_i (1 - \beta_{Ti}^2)^{-1/2}$; q is the 4-momentum of a particle in the frame in which δp_μ

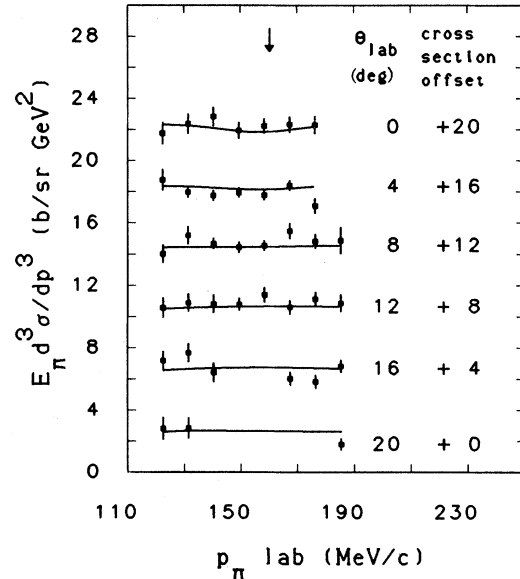
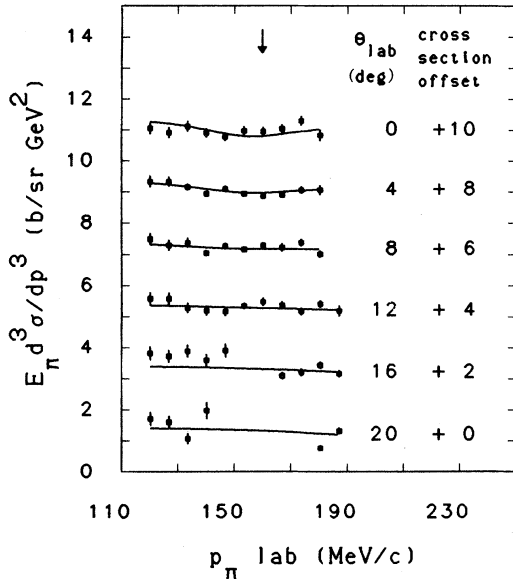
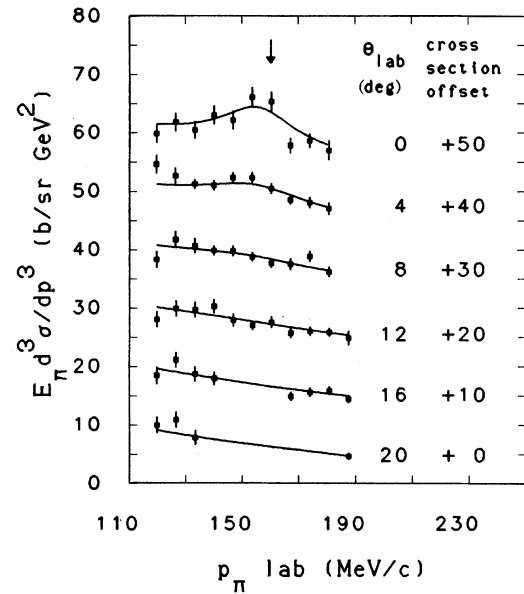
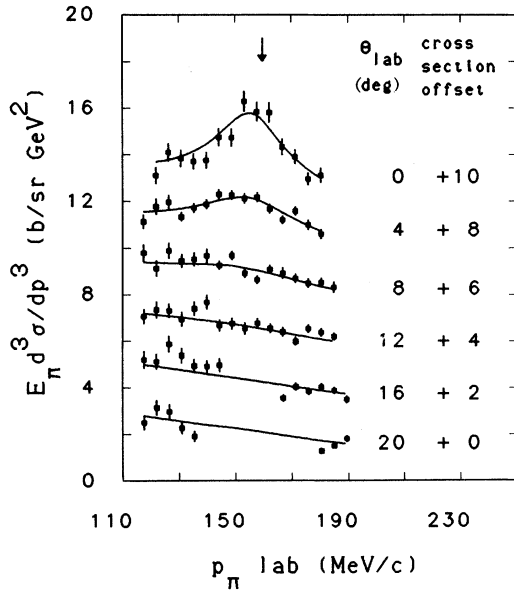


FIG. 14. Lorentz invariant cross section versus laboratory momentum for (a) $\text{Ne} + \text{Cu} \rightarrow \pi^-$ at $E/A=485$ MeV and (b) for $\text{Ne} + \text{Cu} \rightarrow \pi^+$ at $E/A=485$ MeV. See also the caption for Fig. 6.

FIG. 15. Lorentz invariant cross section versus laboratory momentum for (a) $\text{Ne} + \text{U} \rightarrow \pi^-$ at $E/A=487$ MeV and (b) for $\text{Ne} + \text{U} \rightarrow \pi^+$ at $E/A=487$ MeV. See also the caption for Fig. 6.

is being evaluated $= (E/c, \vec{p})$; $p'_i = [(E'_i/c)^2 - (m_\pi c)^2]^{1/2}$; and $\alpha = e^2/\hbar c = \frac{1}{137}$.

We assume

$$R_i = \frac{2}{3} r_0 A_i^{1/3},$$

where A_i is the mass number and r_0 is taken somewhat arbitrarily as 1.4 fm. The factor of $\frac{2}{3}$ relates the mean inverse radius of a uniformly charged

sphere to its radius.

The source function is then modified by a phase space distortion factor as shown in Eq. (1). In that equation

$$\delta D(p) = \pi \alpha \sum_i Z_i \frac{E'_i}{p'_i c} \mathcal{F}(p'_i), \quad (3)$$

where the variables have the same meanings as

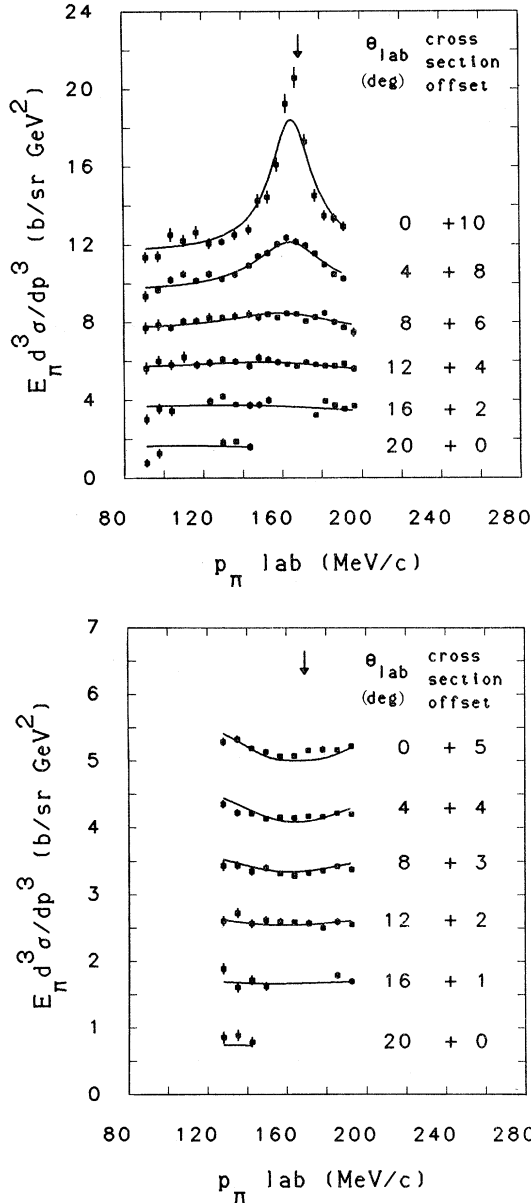


FIG. 16. Lorentz invariant cross section versus laboratory momentum (a) for $\text{Ar} + \text{C} \rightarrow \pi^-$ at $E/A=533$ MeV and (b) for $\text{Ar} + \text{C} \rightarrow \pi^+$ at $E/A=533$ MeV. See also the caption for Fig. 6.

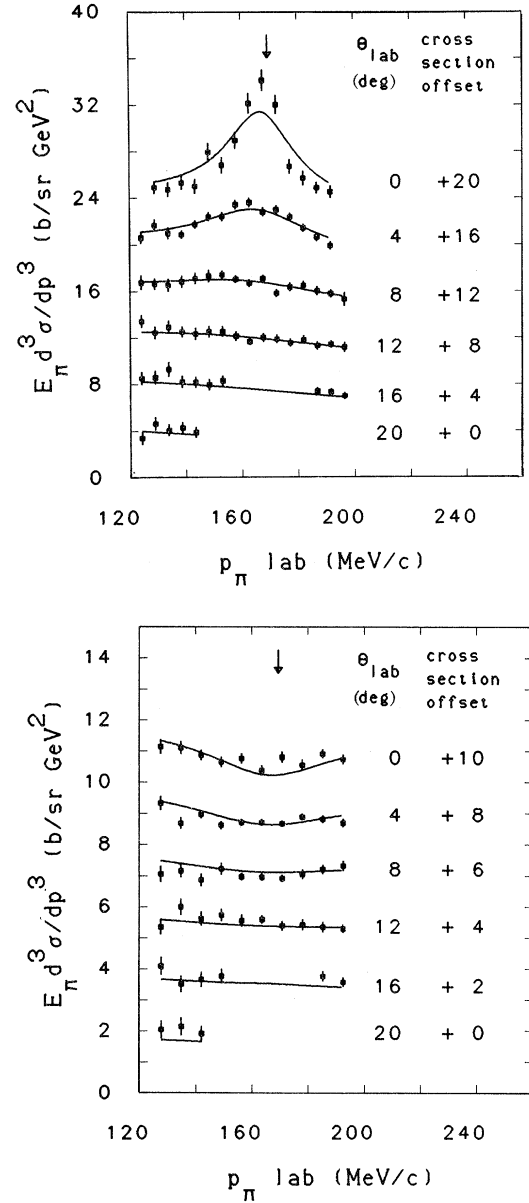


FIG. 17. Lorentz invariant cross section versus laboratory momentum for (a) $\text{Ar} + \text{KCl} \rightarrow \pi^-$ at $E/A=534$ MeV and (b) for $\text{Ar} + \text{KCl} \rightarrow \pi^+$ at $E/A=534$ MeV. See also the caption for Fig. 6.

above, and for the form factor we take

$$\mathcal{F}(p_i') = [(\pi p_i' R / \hbar)^2 + 1]^{-1/2}.$$

Notice that as $p \rightarrow 0$, $\delta D / \pi$ reduces to the conventional form for the Sommerfeld parameter ($\eta = Z\alpha/\beta$). Our form factor is not identical to that derived by GK for an exponential charge distribution, but it closely approximates their expres-

sion, has the same limits as $p \rightarrow 0$ and $p \rightarrow \infty$, and is simpler to evaluate.

The sums in Eqs. (2) and (3) are over all charge distributions. We assume that there are projectile and target fragments with charges Z_p and Z_t at relatively low temperatures. Temperatures are parametrized in terms of a thermal velocity (β_{Ti}) as shown below Eq. (2). A hot central charge dis-

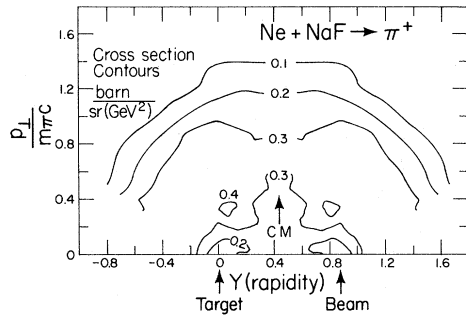


FIG. 18. Contours of Lorentz invariant cross section ($E_\pi d^3\sigma/dp_\pi^3$) on a rapidity [$y = \tanh^{-1}(p_{\parallel}/E)$] vs p_{\perp} plot for Ne + NaF at $E/A = 380$ MeV. The present results have been combined with the data of Nakai *et al.* (Ref. 3) at larger angles to produce this plot. The cross sections from Nakai *et al.* have been multiplied by a factor of $\frac{3}{4}$ to correct for the difference between our normalization and theirs.

tribution is assumed for all of the charge not contained in the projectile and target fragments.

It was not possible to fit our data or those of Ref. 7 with an uncharged source function of a single Boltzmann distribution (the fireball model²¹) since, in contrast to the predictions of that model,

the measured differential cross section ($d^3\sigma/dp^3$) does not always fall with increasing pion energy in the center of mass. We used a source expressed by the lowest three terms in a momentum expansion about the center of mass. A Boltzmann factor exponential with pion "temperature" estimated from Nagamiya *et al.*¹ was used to give the correct asymptotic behavior.

$$\sigma_0(p, \theta) = N \left[1 + \left(\frac{p_{c.m.}}{m_{\pi}c} \right)^2 (c_1 + c_2 P_2[\cos\theta_{c.m.}]) \right] \times \exp(-E_{c.m.}/T), \quad (4)$$

where $p_{c.m.}$, $E_{c.m.}$ are the momentum and total energy (mass plus kinetic) of the pion in the nucleon-nucleon center of mass; N is the normalization parameter; c_1, c_2 are the source shape parameters; $P_2(\cos\theta) = (3\cos^2\theta - 1)/2$, and T is the slope parameter or temperature of the source. For $c_1 = c_2 = 0$, this expression reduces to a central thermal pion source. Notice that the temperature in Eq. (4) is not equal to the temperature in Eqs. (2) and (3).

TABLE III. Widths and momentum shifts of peaks in π^- spectra.

E_{beam}/A (MeV)	Beam	Target	dp_{\parallel}^a (MeV/c)	$\Gamma_{\parallel}/2^b$ (MeV/c)	$\Gamma_{\perp}/2^c$ (MeV/c)
280	²⁰ Ne	C	3.0	7	10
281	²⁰ Ne	NaF	3.5	8	10
282	²⁰ Ne	Cu	4.0	9	13
380	²⁰ Ne	NaF	3.5	9	8
382	²⁰ Ne	Cu	3.5	11	11
385	²⁰ Ne	U	3.5	12	10
482	²⁰ Ne	C	3.0	8	10
483	²⁰ Ne	NaF	3.0	8	10
485	²⁰ Ne	Cu	2.5	9	10
487	²⁰ Ne	U	2.5	13	13
533	⁴⁰ Ar	C	2.5	5	7
534	⁴⁰ Ar	KCl	1.5	6	11

^aShift of the center of the peak in the π^- spectrum from the incident beam velocity, measured in the beam velocity reference frame.

^bHalf-width at half-maximum (measured from a smooth background) of the peak in the π^- spectrum in the p_{\parallel} direction, corrected for experimental resolution. Measured in the beam velocity reference frame.

^cHalf-width at half-maximum (measured from a smooth background) of the peak in the π^- spectrum in the p_{\perp} direction, corrected for experimental resolution.

B. Parameters for least squares fits

The normalization [N in Eq. (4)], the source shape parameters [c_1 and c_2 in Eq. (4)], and the charge on the projectile fragment (Z_p) were used as parameters in a least squares fit of this function to our data. The shift of the peak in the π^- spectrum (or hole in the π^+ spectrum) from the velocity of the incident projectile ($dp_{||}$ values in Table III) was estimated graphically and was held fixed during the fitting procedure.

The charge on the target fragment was calculated by assuming that the same number of nucleons were knocked out of the target as were knocked out of the projectile. The charge-to-mass ratio of both the projectile and target fragments were assumed to be the same as in the initial nuclei. The charge and mass of the hot central charge distribution were then calculated by charge and baryon number conservation. The charge of the produced pion was included in the charge balance equation. For the projectile and target fragments, we have fixed the parameter β_{Ti} according to measured velocity dispersion of projectile fragments²²⁻²⁴ [see Eq. (6) below]. The temperature [in Eqs. (2) and (3)] of the central charge distribution was taken to be $T = 2E^*/3$, where E^* is the beam energy per nucleon in the center of mass. Source shape parameters c_1 and c_2 for π^+ were taken from corresponding π^- fits. In Table IV and Figs. 19 and 20 we show the values of the parameters found in our fits. The uncertainties associated with the parameters are defined in the Appendix.

C. Results of fits

The solid curves of Figs. 2–17 show the results of these fits. The resolution of the spectrometer has been folded into these curves. The dashed lines in Figs. 2–5 show the same fitting function before folding with the resolution, and the dotted lines show the uncharged pion source function [see Eq. (4)]. The fits were made as a function of momentum and angle, so the comparisons of the calculations and the data in Figs. 2–5 represent only two cuts through the two-dimensional surface centered on the π^- peak and π^+ hole near beam velocity.

A few words are necessary to explain the physical interpretation we attach to β_{Ti} , GK's thermal expansion velocity for a cool, but thermally expanding unbound projectile remnant. In addition to the fitting listed in Table IV we attempted to fit

β_{Ti} as a free parameter. The β_T values for the projectile fragment so obtained correspond to nucleon temperature values that are unreasonably small, of the order of 1 MeV, which implies that the projectile fragment will be bound and will not expand. These results prompted us to formulate quantitatively the role of bound projectile fragments near beam velocity. In a separate paper Radi *et al.*²⁵ have derived expressions for the projectile fragment Coulomb effects. One such expression may be written for pions near the beam velocity as

$$\delta D(\beta_\pi) = \pm \pi Z \alpha / (\beta_\pi^2 + \beta_T^2)^{1/2}. \quad (5)$$

In the nonrelativistic limit, Eq. (3) reduces to Eq. (5) if the form factor is taken at its limit of unity (corresponding to beam velocity pions) and β_π is the pion velocity (in units of c) in the projectile spectator reference frame. Our interpretation of the meaning of β_T is quite different from that of GK. In our case β_T is the rms velocity dispersion of the projectile fragments instead of the rms thermal expansion velocity of a charge cloud.

The velocity (momentum) dispersion of projectile fragments has been studied for several projectile particles and energies.²²⁻²⁴ The parallel momentum dispersion has been fit by the general expression

$$\langle p_{||}^2 - \langle p_{||} \rangle^2 \rangle^{1/2} = \sigma_0 \left[\frac{A_F(A - A_F)}{A - 1} \right]^{1/2}, \quad (6)$$

where A is the mass of the projectile and A_F the mass of the fragment. Table V lists the values of σ_0 for the systems studied in Refs. 22–24.

We assume the constant 86 MeV/ c for our work, although the pion-associated fragments may not be representative of the inclusive fragmentation σ_0 value. The parameter β_T used in our fitting procedure was calculated using an expression of the same form as Eq. (6). Specifically, we assumed

$$\beta_T = \frac{0.16}{A_F} \left[\frac{A_F(A - A_F)}{A - 1} \right]^{1/2}, \quad (7)$$

where $0.16 = \sqrt{3}\sigma_0/931.5$ MeV. The factor $\sqrt{3}$ was obtained by assuming that the momentum dispersion of the two components perpendicular to the beam was the same as the parallel dispersion, then adding the three components in quadrature. The mass numbers in this equation were calculated from the charges by assuming that the charge-to-mass ratios of the projectile and target fragments were the same as the original nuclei.

TABLE IV. Parameters from least square fitting of pion data.

E/A (MeV)	Beam	Target	Z_{eff}^a		$N \frac{\mu b}{\text{MeV}^3}^b$		$\sigma_{\text{tot}}(\text{mb})^c$		T^d (MeV)	c_1^e		c_2^e		χ^2/N^f	
			π^+	π^-	π^+	π^-	π^+	π^-		π^+	π^-	π^+	π^-		
280	^{20}Ne	C	3.8 ± 0.2	6.4 ± 0.2	0.11 ± 0.01	0.11 ± 0.01	25	25	30	2.9 ± 0.5	0.0 ± 0.4	2.06	1.74		
281	^{20}Ne	NaF	3.1 ± 0.2	5.6 ± 0.2	0.16 ± 0.01	0.19 ± 0.01	30	35	30	2.1 ± 0.6	1.0 ± 0.5	1.33	2.00		
282	^{20}Ne	Cu	1.8 ± 0.3	4.3 ± 0.3	0.40 ± 0.02	0.47 ± 0.04	58	69	30	1.4 ± 0.7	1.3 ± 0.7	1.12	1.64		
380	^{20}Ne	NaF	3.3 ± 0.1	4.6 ± 0.1	0.15 ± 0.01	0.20 ± 0.01	85	113	36	1.7 ± 0.1	0.0 ± 0.1	2.28	2.63		
382	^{20}Ne	Cu	2.3 ± 0.1	3.4 ± 0.1	0.37 ± 0.01	0.43 ± 0.02	169	194	36	1.1 ± 0.2	0.0 ± 0.1	1.29	1.58		
385	^{20}Ne	U	1.5 ± 0.3	2.7 ± 0.2	0.91 ± 0.04	1.62 ± 0.15	292	521	36	0.6 ± 0.2	0.0 ± 0.1	0.94	1.47		
482	^{20}Ne	C	3.5 ± 0.1	5.0 ± 0.1	0.08 ± 0.01	0.09 ± 0.01	149	155	45	1.1 ± 0.2	0.0 ± 0.1	2.10	1.44		
483	^{20}Ne	NaF	2.9 ± 0.1	4.4 ± 0.1	0.14 ± 0.01	0.16 ± 0.01	217	243	45	0.8 ± 0.1	0.0 ± 0.1	1.86	2.16		
485	^{20}Ne	Cu	2.2 ± 0.1	3.5 ± 0.1	0.31 ± 0.01	0.43 ± 0.01	184	253	45	0.0 ± 0.1	0.2 ± 0.1	2.38	2.06		
487	^{20}Ne	U	1.8 ± 0.3	3.1 ± 0.2	0.63 ± 0.03	1.54 ± 0.04	374	913	45	0.0 ± 0.1	0.0 ± 0.1	1.17	1.02		
533	^{40}Ar	C	8.4 ± 0.4	6.3 ± 0.1	0.12 ± 0.01	0.16 ± 0.01	300	420	50	0.7 ± 0.1	0.0 ± 0.1	2.73	2.36		
534	^{40}Ar	KCl	4.2 ± 0.3	4.4 ± 0.2	0.27 ± 0.01	0.44 ± 0.01	339	558	50	0.1 ± 0.1	0.0 ± 0.1	1.76	1.42		

^aEffective charge of projectile fragment.

^bNormalization parameter in Eq. (4).

^cThe uncharged pion source function integrated over all momenta and angles. Notice that the source function is symmetric about the center of mass, so this is not a good measure of the total cross section except for equal mass collisions. In the asymmetric cases, this is still given in order to put the normalization in familiar units.

$$\sigma_{\text{tot}} = 4\pi N m_{\pi}^3 \left[\frac{T}{m_{\pi}} \right] \left[K_2 \left[\frac{m_{\pi}}{T} \right] + \frac{3c_1 T}{m_{\pi}} K_3 \left[\frac{m_{\pi}}{T} \right] \right],$$

where K_2 and K_3 are modified Bessel functions and the other parameters are defined as in Eq. (4).

^dThe temperature in the Boltzmann factor of the uncharged pion source function [Eq. (4)]. Estimated from the data of Ref. 1.

^e c_1, c_2 = source shape parameters in Eq. (4). A zero value means less than 10^{-5} .

^f χ^2/N = chi-square per degree of freedom in the fit. The number of degrees of freedom for a given set of data ranges from 39 to 126, with an average of 70.

Further evidence that the pion focusing or defocusing near beam velocity is associated with bound fragments comes from the downshift of the peaks. For the ^{20}Ne beam the π^- peak is consistently downshifted from beam velocity by 3.2 ± 1.6 MeV/c (projectile frame). The π^+ depression downshift is less well defined but is about the same as π^- . Van Bibber *et al.*²⁴ state that the mean energy of fragments is downshifted by about 10 MeV per nucleon, which is equivalent to pion momentum shift in the projectile frame of 3.4 MeV/c. Greiner *et al.*²² measured the momentum shifts of the beam fragments at higher beam energies where they are about a factor of 3 smaller than the shift measured by Van Bibber *et al.* Our data at intermediate bombarding energies lie closer to the shifts measured at the lower beam energies. The accuracy associated with the 10 MeV per nucleon downshift reported by Van Bibber *et al.* was not specified, but because an exact number was not given

and because the uncertainty associated with the downshift of the π^- peak is large, conclusions concerning the agreement or disagreement of the two numbers must be treated with caution. It is also possible that pion producing reactions are associated with a larger downshift than is associated with normal fragmentation.

Van Bibber *et al.*²⁴ show that the momentum dispersion perpendicular to the beam exceeds the parallel dispersion at 92.5 and 117.5 MeV per nucleon, and this feature is attributed to orbital deflection. This anisotropy is expected to decrease with increasing bombarding energy, and Greiner *et al.*²² specifically state the dispersion is isotropic within 10% at 1 and 2 GeV/N. The fits shown on Figs. 2–17 have assumed that the momentum dispersion of the beam fragments is isotropic. However, a careful examination of some of our figures indicates a slight anisotropy in that the width in the perpendicular direction slightly exceeds that

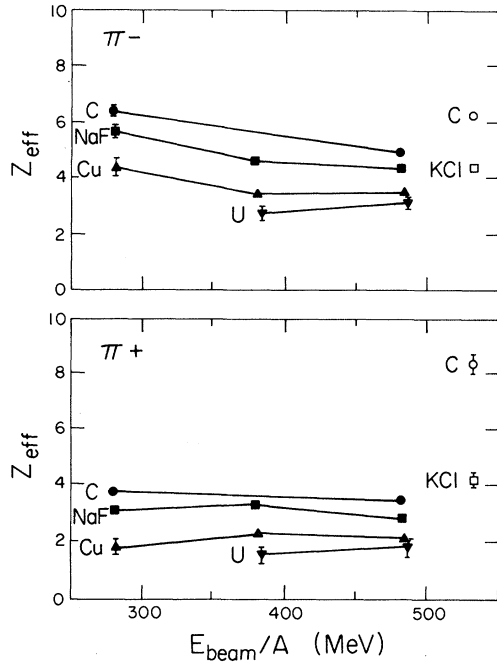


FIG. 19. Effective charge of the projectile fragment from the least squares fits of the Coulomb correction formulas (Ref. 10) to the π^- (top) and π^+ (bottom) data. The closed symbols are from the data with Ne beams and the open symbols with an Ar beam. The lines are to guide the eye. The target is shown next to each point or set of points.

in the parallel direction. A more quantitative measure of the systematic sideward anisotropy of the beam velocity π^- peak is seen in Table III by comparison of the half-widths $\Gamma_i/2$, corrected for experimental resolution. This anisotropy is most pronounced for the lowest energy ($E/A=280$

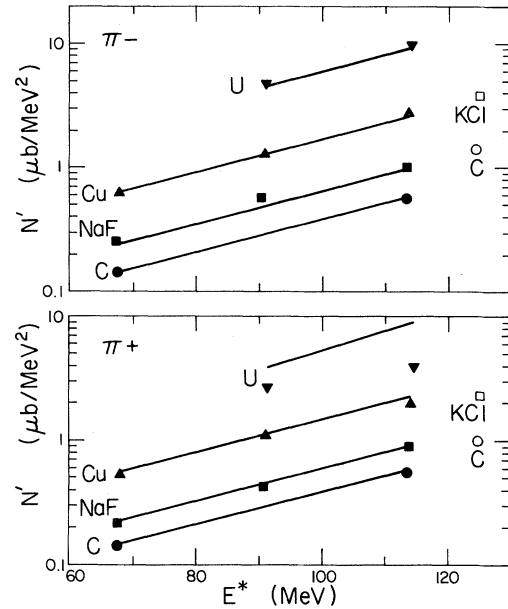


FIG. 20. The values of the Lorentz invariant form of the uncharged pion source function [Eq. (4)] evaluated for pions at rest in the center of mass [$N' = m_\pi \sigma_0(p_{c.m.} = 0) = Nm_\pi \exp(-m_\pi/T)$] vs beam energy per nucleon in the center of mass. The closed symbols are for a Ne beam and the open symbols for an Ar beam. The lines are from a semiempirical parametrization of these values [see Eq. (8)]. The target is shown next to each point or set of points.

MeV) Ne data and for the Ar data. That the π^- peak anisotropy qualitatively follows the projectile fragment anisotropy is further evidence that the Coulomb focusing by projectile fragments governs the π^- peak.

The effective projectile fragment Z values of

TABLE V. Momentum dispersion of projectile fragments.

Authors	E/A (MeV)	Beam	Target	σ_0 (MeV/c)
Greiner <i>et al.</i> (Ref. 22)	1050	^{12}C	various ^a	70 ± 2^b
	2100	^{12}C	various ^a	74 ± 2^b
	2100	^{16}O	various ^a	86 ± 2^b
Viyogi <i>et al.</i> (Ref. 23)	213	^{40}Ar	C	94 ± 5
Van Bibber <i>et al.</i> (Ref. 24)	92.5	^{16}O	Al	86
	92.5	^{16}O	Au	80

^aAveraged over targets from Be to Pb. The authors say that σ_0 does not depend on target mass above the 5% level.

^bNotice that their definition of σ_0 differs from our definition by a factor of 2; the values of σ_0 quoted here are one-half of the values given in the original reference.

Table IV and Fig. 19 show a slight decrease with bombarding energy for the lighter targets, reversing for heavy targets. For the nearly equal mass Ne-NaF collisions, the Z values for π^- are typically about half the initial charge of the neon beam, while the values for π^+ are more nearly a third of the initial charge. As the mass of the target increases, the effective Z value consistently decreases for both π^+ and π^- . For the neon beam the effective charge on the projectile fragment for π^+ is less than for π^- for all targets which were used. This difference can be qualitatively understood in that a beam velocity π^+ arises from a smaller average impact parameter than π^- , as noted by GK.¹⁰ The difference could have another explanation. By charge conservation, the charge of the remaining particles will be two units less when a π^+ is produced than when a π^- is produced. The division of these two charges among the rest of the system depends upon the pion production mechanism, but it is interesting to notice that Z_{eff} for π^+ is generally about two less than for π^- . This difference between π^+ and π^- is not seen for the argon beam. However, the fitting procedure has not been as successful for argon as for neon projectiles. The peak in the fit to the π^- spectrum is not as sharp as the data and the depression in the fit to the π^+ spectrum is too sharp.

The values of the normalization parameter in the uncharged pion source function [N in Eq. (4)] found by the fitting procedure are given in Table IV. As in the fireball model,²¹ these values of N are almost independent of beam energy, suggesting that it is just a geometric factor. To illustrate the beam energy dependence of Eq. (4) and to display it in a manner independent of the parameters c_1 and c_2 , Fig. 20 shows the values of the Lorentz invariant form of the uncharged pion source function ($Ed^3\sigma/dp^3$) evaluated for pions at rest in the center of mass

$$[N' \equiv m_\pi \sigma_0(p_{\text{c.m.}}=0) = Nm_\pi \exp(-m_\pi/T)]$$

versus the kinetic energy per nucleon of the beam in the center of mass (E^*). Since N is nearly independent of beam energy, the beam energy dependence of N' is contained in the Boltzmann factor $\exp(-m_\pi/T)$. We have found that the values of N' can be parametrized by the simple semiempirical expression

$$N'_\pm = N_0 Y_\pm \exp(E^*/B), \quad (8)$$

where

$$Y_+ = \pi r_0^2 (Z_p A_t^{2/3} + Z_t A_p^{2/3}),$$

$$Y_- = \pi r_0^2 (N_p A_t^{2/3} + N_t A_p^{2/3}),$$

and A_t, Z_t, N_t is the number of nucleons, protons, and neutrons in the target, and A_p, Z_p, N_p is the number of nucleons, protons, and neutrons in the projectile. The geometric factor Y is discussed and described elsewhere.^{1,21,26,27} Using Eq. (8) with $r_0 = 1.2$ fm, $N_0 = (616 \text{ MeV}/c)^{-3}$, and $B = 33$ MeV, the lines shown in Fig. 20 can be calculated. The lines fit reasonably all the points except the Ne + U \rightarrow π^+ data.

The values of c_1 , which are related to the departure of the source function [Eq. (4)] from a Boltzmann distribution, consistently decrease with increasing target mass and with increasing beam energy. Because the calculated cross section can be negative for c_1 less than zero, we have restricted it to positive values. When c_2 is zero, the source function is isotropic in the center of mass. A positive value of c_2 indicates a source function that is forward-backward peaked in the center of mass. We have restricted c_2 to positive values to avoid sideward peaking of the source function and because the calculated cross section can be negative for c_2 less than zero. The fitted values of c_2 are generally consistent with zero, but they are poorly determined since our data are concentrated at low center of mass angles.

Some of the failures in the fitting procedure are probably due to the use of a single value for the projectile fragment charge. An implicit assumption involved in the fitting is that after impact parameter averaging the Coulomb effects can be represented by functions for some average impact parameter. The observed charged pion spectra arise from an impact parameter averaging in which the fragment yield falls off monotonically below the projectile Z , but the probability of pion production must rise with the decreasing projectile fragment charge (i.e., more central collisions). We have replaced this averaging procedure with a function of a single effective charge. This approximation seems to fail for the argon beam. With the detailed averaging procedure of Ref. 25 satisfactory fits are obtained for both Ne + C and Ar + C systems.

V. CONCLUSIONS

In summary, strong Coulomb effects on the charged pion spectra are observed near the beam velocity and, by inference, near the target velocity. For light target-projectile combinations, these ef-

fects can be explained quantitatively in terms of Coulomb interactions between the pions and cold projectile fragments using Gyulassy and Kauffmann's¹⁰ Coulomb correction formulas. Our treatment of the Coulomb effects differs from that of Gyulassy and Kauffmann in that a different expression has been used for the uncharged pion source function [see Eq. (4)]. We also reinterpret their formulas for thermal averaging in terms of an average over the velocity dispersion of the projectile fragments. The shift of the peak in the π^- spectra from the incident beam velocity and the approximate width of these peaks are consistent with previously measured projectile fragmentation data.²²⁻²⁴ We have also seen that the effective charge of the projectile fragment is less for π^+ near beam velocity than for π^- . This difference is consistent with our expectation that positive pions near beam velocity tend to come from more central collisions. Using the same methods, qualitative agreement is achieved for heavier targets and projectiles. The differences between our fitting function and the data are due, at least in part, to an incomplete treatment of impact parameter averaging.

Our data cover a relatively small region of pion momenta and angles, but this band includes the region in which the Coulomb effects are expected to be greatest. In order to understand more exotic phenomena associated with the charged particle spectra in heavy ion interactions, these Coulomb effects must be understood in all momentum regions and taken into account.

ACKNOWLEDGMENTS

Thanks are owed to P. J. Siemens and M. Gyulassy for useful suggestions and discussions. This work was supported by the Office of Energy Research, Division of Nuclear Physics of the Office of High Energy and Nuclear Physics of the U. S. Department of Energy under Contract W-7405-ENG-48, by the INS-LBL collaboration program, Institute for Nuclear Study, University of Tokyo, Japan, and by the U. S. National Science Foundation under Grant No. PHY 78-22696.

APPENDIX

The uncertainty associated with each parameter in Table IV was determined by calculating how much the parameter had to be changed, with all the other parameters freely adjustable, in order to increase the chi squared (χ^2) by one from its value at the minimum.²⁸ These errors are due to the statistical uncertainties in the data. They do not include uncertainties due to any systematic errors in the data or due to the assumptions involved in the fitting expression. Because the source shape parameters [c_1 and c_2 in Eq. (4)] for the π^+ fits were taken from the corresponding π^- fits, the number of parameters that were varied during the complete error analysis was smaller for π^+ than for π^- .

As a result, the errors associated with the π^+ parameters are generally smaller than for π^- . The errors given for c_1 and c_2 are from the π^- fit.

*Present address: Cyclotron Institute, Texas A&M University, College Station, Texas.

†Present address: Physik Institute der Universität Zürich, Zürich, Switzerland.

‡Present address: Boston University, Boston, Massachusetts.

¹S. Nagamiya, M.-C. Lemaire, E. Moeller, S. Schnetzer, G. Shapiro, H. Steiner, and I. Tanihata, *Phys. Rev. C* **24**, 971 (1981).

²J. Chiba, K. Nakai, I. Tanihata, S. Nagamiya, H. Bowman, J. Ingersoll, and J. O. Rasmussen, *Phys. Rev. C* **20**, 1332 (1979).

³K. Nakai, J. Chiba, I. Tanihata, M. Sasao, H. Bowman, S. Nagamiya, and J. O. Rasmussen, *Phys. Rev. C* **20**, 2210 (1979).

⁴K. L. Wolf, H. H. Gutbrod, W. G. Meyer, A. M. Poskanzer, A. Sandoval, R. Stock, J. Gosset, C. H. King, G. King, Nguyen Van Sen, and G. D. Westfall, *Phys. Rev. Lett.* **42**, 1448 (1979).

⁵J. Papp, J. Jaros, L. Schroeder, J. Staples, H. Steiner, A. Wagner, and J. Wiss, *Phys. Rev. Lett.* **34**, 601 (1975); J. Papp, LBL Report LBL-3633, 1975.

⁶S. Y. Fung, W. Gorn, G. P. Kiernan, F. F. Leu, J. J. Lu, Y. T. Oh, J. Osawa, R. T. Poe, L. Schroeder, and H. Steiner, *Phys. Rev. Lett.* **40**, 292 (1978).

⁷W. Benenson, G. Bertsch, G. M. Crawley, E. Kashy, J. A. Nolen, Jr., H. Bowman, J. G. Ingersoll, J. O. Rasmussen, J. Sullivan, M. Koike, M. Sasao, J. Péter, and T. E. Ward, *Phys. Rev. Lett.* **43**, 683 (1979); **44**, 54 (1980).

⁸G. Bertsch, *Nature* **283**, 280 (1980).

⁹K. G. Libbrecht and S. E. Koonin, *Phys. Rev. Lett.* **43**, 1581 (1979); J. Cugnon and S. E. Koonin, *Nucl. Phys.* **A355**, 477 (1981).

¹⁰M. Gyulassy and S. K. Kauffmann, *Nucl. Phys.* **A362**, 503 (1981).

¹¹C. M. Ko and P. J. Siemens, *Nucl. Phys.* **A367**, 496 (1981).

- ¹²E. M. Friedländer, *Phys. Lett* **2**, 38 (1962).
- ¹³N. I. Kostanashvili, G. I. Lebedevich, and D. S. Nabichvrishvili, *Yad. Fiz.* **13**, 1243 (1971) [*Sov. J. Nucl. Phys.* **13**, 715 (1971)].
- ¹⁴J. Burfening, E. Gardner, and C. M. G. Lattes, *Phys. Rev.* **75**, 382 (1949).
- ¹⁵H. Yagoda, *Phys. Rev.* **85**, 891 (1952).
- ¹⁶J. C. Alder, B. Gabioud, C. Joseph, J. F. Loude, N. Morel, A. Perrenoud, M. T. Tran, B. Vaucher, E. Winkelmann, D. Renker, H. Schmitt, C. Zupancic, H. Von Fellenberg, A. Frischknecht, F. Hoop, G. Strassner, and P. Truöl, *Nucl. Instrum. Methods* **160**, 93 (1979).
- ¹⁷A. S. Carroll, I. H. Chiang, C. B. Dover, T. F. Kycia, K. K. Li, P. O. Mazur, D. N. Michael, P. M. Mockett, D. C. Rahm, and R. Rubenstein, *Phys. Rev. C* **14**, 635 (1976).
- ¹⁸K. Frankel, J. Bistirlich, H. Bowman, R. Bossingham, K. M. Crowe, C. J. Martoff, D. Murphy, J. Rasmussen, J. Sullivan, W. Zajc, O. Hashimoto, M. Koike, J. Peter, W. Benenson, G. M. Crawley, E. Kashy, and J. A. Nolen, Jr., *Phys. Rev. C* **25**, 1102 (1982).
- ¹⁹R. Wada and J. R. Alonso, *IEEE Trans. Nucl. Science* **NS-28**, 2276 (1981).
- ²⁰J. P. Sullivan, Ph.D thesis, University of California, Berkeley, LBL Report LBL-12546, 1981 (unpublished).
- ²¹J. I. Kapusta, *Phys. Rev. C* **16**, 1493 (1977).
- ²²D. E. Greiner, P. J. Lindstrom, H. H. Heckman, Bruce Cork, and F. S. Bieser, *Phys. Rev. Lett.* **35**, 152 (1975).
- ²³Y. P. Viyogi, T. J. M. Symons, P. Doll, D. E. Greiner, H. H. Heckman, D. L. Hendrie, P. J. Lindstrom, J. Mahoney, D. K. Scott, K. Van Bibber, G. D. Westfall, H. Wieman, H. J. Crawford, C. McParland, and C. K. Gelbke, *Phys. Rev. Lett.* **42**, 33 (1979).
- ²⁴K. Van Bibber, D. L. Hendrie, D. K. Scott, H. H. Wieman, L. S. Schroeder, J. V. Geaga, S. A. Chessin, R. Treuhaft, Y. J. Grossiord, J. O. Rasmussen, and C. Y. Wong, *Phys. Rev. Lett.* **43**, 840 (1979).
- ²⁵H. M. A. Radi, J. O. Rasmussen, J. P. Sullivan, K. A. Frankel, and O. Hashimoto, LBL Report LBL-12591, 1981.
- ²⁶R. J. Glauber and G. Matthiae, *Nucl. Phys.* **B21**, 135 (1970).
- ²⁷J. Hüfner and J. Knoll, *Nucl. Phys.* **A290**, 460 (1977).
- ²⁸Both the fitting and the error analysis were done with the MINUIT program (version 2.77) written at CERN. A description of this program, the minimization methods used (see the section on MIGRAD), and the error analysis (see the section on MINOS) are available from: Program Library, Division DD, CERN, CH 1211 Geneva 23, Switzerland. Ask for the long write-up on MINUIT, D506.